# On Large-Strain Inelastic Torsion of Glassy Polymers

Wu, P.D.; van der Giessen, Erik

*Published in:*
International Journal of Mechanical Sciences

*DOI:*
10.1016/0020-7403(93)90031-O



*Publication date:*
1993

*Int. J. Mech. Sci.* Vol. 35, No. 11, pp. 935–951, 1993
Printed in Great Britain.

0020-7403/93 $6.00 + .00


# ON LARGE-STRAIN INELASTIC TORSION OF GLASSY POLYMERS

P. D. WU and E. VAN DER GIESSEN
Laboratory for Engineering Mechanics, Delft University of Technology, P.O. Box 5033, 2600GA, Delft, The Netherlands

(*Received* 25 *November* 1992; *and in revised form* 19 *April* 1993)

**Abstract**—Large-strain elastic–viscoplastic torsion of circular tubes and solid bars of glassy polymers is investigated under fixed-end as well as free-end conditions. The analysis employs a large inelastic deformation model for glassy polymers that incorporates a recently proposed constitutive law for the so-called orientational hardening, which is identified to play a key role in the description of the deformation-induced anisotropy in glassy polymers. The solution of the problem is obtained numerically by means of simple, special purpose finite elements. Results are presented in terms of predicted torque vs twist curves for all cases. Furthermore, we present axial force vs twist curves for fixed-end torsion or elongation vs twist curves for free-end torsion, both phenomena being associated with anisotropic hardening. In some cases, the predicted stress distributions are also given. The differences between free-end and fixed-end torsion are emphasized. Numerical results predicted by the model are compared with experimental results for polycarbonate found in the literature.

## NOTATION

*General*

| | |
|---|---|
| $\mathbf{a}, \mathbf{A}$ | second-order tensor |
| $\mathbf{A}$ | fourth-order tensor |
| A | matrix or column matrix (vector) |
| $(\dot{})$ | material time derivative or rate |
| $(^{\nabla})$ | Jaumann rate |
| $(')$ | deviatoric part |
| $(_0)$ | initial value |
| $(_v)$ | instantaneous rate term from viscoplasticity |
| $(\ )^T$ | transpose of tensor or matrix |
| $(\ )^{-1}$ | inverse of a tensor or matrix |
| tr | trace of a second-order tensor or matrix |

*Variables*

| | |
|---|---|
| $A$ | material constant in viscoplastic flow rule |
| $\mathbf{B}, B_i$ | back stress tensor and its principal components |
| $B_i^{3-\mathrm{oh}}$ | principal back stresses according to three-chain model |
| $B_i^{8-\mathrm{ch}}$ | principal back stresses according to eight-chain model |
| $C^{\mathrm{R}}$ | rubbery modulus |
| $\mathbf{D}^{\mathrm{p}}, \mathbf{D}$ | plastic strain-rate and total strain-rate tensors |
| $E$ | Young's modulus |
| $\dot{\mathrm{E}}$ | column matrix (vector) of generalized element strain rates |
| $\mathbf{e}_i$ | Cartesian base vector |
| $\mathbf{e}_i^{\mathrm{p}}$ | base vectors of Eulerian triads |
| $e$ | stretch of specimen in axial direction |
| $F$ | axial force |
| F | force column matrix (vector) |
| $\mathbf{F}^{\mathrm{e}}, \mathbf{F}^{\mathrm{p}}, \mathbf{F}$ | elastic, plastic and total deformation gradient tensors |
| $h$ | material constant in softening law |
| $J$ | change of volume |
| $\mathbf{L}^{\mathrm{e}}, \mathbf{L}^{\mathrm{p}}, \mathbf{L}$ | elastic, plastic and total velocity gradient tensors |
| $\mathbf{L}_{\mathrm{e}}$ | elastic moduli |
| $L$ | current length of the specimen |
| $M$ | torque |
| $m_i^0$ | unit vector components in orientation space |
| $N, n$ | network parameters |
| $p, \alpha$ | pressure and pressure dependence coefficient |

| | |
|---|---|
| $\mathbf{R}$ | rotation tensor |
| $R_i$, $R_o$ | inner radius and outer radius of the bar |
| $r$, $\theta$, $z$ | cylindrical coordinate system |
| $s$, $s_0$, $s_{ss}$ | shear strength and its initial and saturation values |
| $T$ | absolute temperature |
| $\Delta t$ | time increment |
| $U$ | axial displacement |
| $\mathbf{V}^p$, $\mathbf{V}$ | plastic stretch and total stretch tensors |
| $\mathbf{v}$ | velocity vector |
| v | column matrix (vector) of degrees of freedom |
| $V^e$ | volume of the element |
| $\mathbf{W}^p$, $\mathbf{W}$ | plastic spin and continuum spin tensors |
| $\dot{\gamma}_0$ | material parameter in viscoplastic flow rule |
| $\dot{\gamma}^p$, $\mathbf{N}$ | magnitude and direction of plastic strain rate |
| $\mu$ | elastic shear modulus |
| $\nu$ | Poisson's ratio |
| $\tau$ | effective shear stress |
| $\boldsymbol{\sigma}$, $\sigma_{ij}$ | Cauchy stress tensor and its physical components on $\mathbf{e}_i$ |
| $\boldsymbol{\sigma}^*$ | driving stress tensor |
| $\Sigma$ | column matrix (vector) of generalized stresses |
| $\lambda_i^p$, $\lambda_{max}^p$ | principal plastic stretches and their maxima |
| $\mathscr{L}$ | Langevin function |
| $\rho_p$ | network model parameter |
| $\psi$, $\varphi$ | twist per unit length, torsion angle |
| $\zeta$ | local coordinate in finite element |
| $\theta_0$, $\varphi_0$ | coordinates in orientation space |
| K, D, S, G | FE stiffness matrix and auxiliary matrices |

## 1. INTRODUCTION

Torsion of a circular bar in the range of large plastic strains has recently been the subject of numerous investigations. One of the main reasons for this is that the torsion test provides an excellent means for obtaining experimental data for the constitutive behaviour of elastic–plastic solids at large to very large deformations. The major advantage over the standard tensile test is that deformations of a solid bar in torsion remain axially homogeneous up to final failure without giving rise to strain localization phenomena such as necking and shear banding. Evidently, torsional deformations are inhomogeneous in the radial direction, but this multiaxiality is lower and more easily tractable than the three-dimensional state inside necks, etc. This has been shown before for the large-strain torsion of metals in Refs [1–5] by means of a numerical method, and will be demonstrated here for glassy polymers.

Although torsion of a circular bar may appear to be a simple deformation process, the so-called Swift effect of notable axial extensions during large-strain torsion of a metal bar with axially free ends—studied first by Swift in 1947 [6]—is a fascinating and complex phenomenon. At room temperature, most initially isotropic metals tend to elongate during torsion when the specimen's ends are axially free (see also Refs [7, 8]). An analogous effect is the development of an axial force when the ends of the bar are axially fixed. It has been firmly established that these axial effects at large plastic strains in polycrystalline metals are due to the development of texture (e.g. Refs [9, 10]). Now, the constitutive modelling of the macroscopic behaviour of elastic–plastic solids, where proper account is given of the induced anisotropy associated with texture development, is currently considered one of the most challenging areas in continuum plasticity theory and has attracted a great deal of interest recently. It has been shown that the predictions of the axial effects show a remarkably strong dependence on the constitutive relations adopted [see e.g. Refs [1–5, 10]). Thus, the torsion test seems to provide a simple yet effective means for assessing the adequacy of such constitutive models.

It has been found that the axial extension effect is more pronounced in thin-walled tubes than in solid bars [8]. In fact, many experimentalists have preferred torsion experiments on tubes over solid bars (see e.g. Ref. [11]). Reducing the wall thickness of a tube will reduce the nonuniformity of the deformation, and if the tubes are extremely thin then the deformation

can be approximated to be homogeneous so that the experimental results can be easily interpreted. In fact, many experimental procedures based on torsion have used thin-walled specimens for which the state of the deformation has been assumed to be completely uniform and, for fixed-end torsion, to be a state of simple shear (see e.g. Ref. [11]). Unfortunately, in order to avoid buckling in a finite-deformation torsion experiment on a hollow tube, it is necessary that the thickness of the tube be at least 10–15% of the mean radius [12]. Therefore, these hollow tubes cannot really be considered to be thin and the deformation is not really homogeneous. In addition to this, a thin hollow tube is much more difficult to manufacture and grip than a solid bar, so that in view of the various experimental problems, thin-walled tubes seem to be of less practical importance at large strains. Consequently, the numerical simulation of both solid bars and (thick-walled) tubes under large-strain torsion, accounting accurately for nonuniform states of deformation, is of considerable practical significance.

It is expected that axial phenomena occur also in large-strain torsion of glassy polymers (see e.g. Ref. [13]). The first finite element simulation of large-strain torsion of glassy polymers was developed very recently by the authors [14]. In that preliminary study, we have considered the solid-bar torsion of polycarbonate (PC) based on a constitutive framework developed by Boyce, Parks and Argon [15]. Their constitutive model incorporates rate- and temperature-dependent plastic flow, softening and subsequent orientational hardening, which are generally considered as key phenomena. We have compared the predictions of the axial effects for three different orientation hardening models, namely the three-chain model [15], the eight–chain model [16, 17] and full network model [18, 19]. It was found that the predictions of the axial effects are sensitive to the orientation hardening relations adopted [14].

In this paper, a numerical analysis of combined torsion and tension of circular solid bars as well as tubes is presented, focussing on both fixed-end and free-end torsion as limiting cases. The approach is based on special purpose, ring-shaped finite elements. These elements are effectively one-dimensional and allow for an efficient analysis of such problems. Differences between the behaviour in free-end and in fixed-end torsion are emphasized. Furthermore, the differences in behaviour of solid bars and of tubes are discussed. Numerical results predicted by the model are compared with experimental results for thick-walled polycarbonate tubes found in Ref. [13].

Tensors will be denoted by bold-face letters. The tensor product is denoted by $\otimes$ and the following operations apply ($\mathbf{a} = a_{ij}\mathbf{e}_i \otimes \mathbf{e}_j$, $\mathbf{b} = b_{ij}\mathbf{e}_i \otimes \mathbf{e}_j$): $\mathbf{ab} = a_{ik}b_{kj}\mathbf{e}_i \otimes \mathbf{e}_j$ and $\mathbf{a}:\mathbf{b} = a_{ij}b_{ij}$, with proper extension to higher-order tensors.

## 2. CONSTITUTIVE EQUATIONS

We start by briefly recapitulating the model for large inelastic deformations of glassy polymers developed by Boyce, Parks and Argon [15], which will be referred to henceforth as the BPA model. The BPA model is developed within an internal variable framework, but at the same time is to a large extent based on the micromechanics and orientation behaviour associated with the molecular chain network structure of polymers and its affine deformation characteristics. In the BPA model, the microstructure of an initially isotropic amorphous polymer is assumed to consist primarily of long molecular chains, which are randomly coiled in space. Side groups protrude from the backbone chains at various locations and, in conjunction with the overall chain trajectory, can act as nodes, or points of physical entanglement. This results in a network-like structure much like that of rubber, but with the chemical crosslinks replaced by physical entanglements.

Following the pioneering work of Haward and Thackray [20], it is assumed that a glassy polymer must overcome two distinct physical sources of resistance before large-strain inelastic flow may occur. Below the glass transition temperature, prior to initial yield, the material must be stressed to exceed its intermolecular resistance to segment rotation. Once the material is free to flow, molecular alignment occurs, resulting in an anisotropic internal resistance to further inelastic deformation, which is called orientational hardening; this will be discussed in Subsection 2.2.

The intermolecular resistance to plastic flow is considered to be due to the impedance imposed by neighbouring chains on the ability of a chain segment to rotate either individually or in a cluster. Based upon the assumption that plastic flow occurs by double-kinking of molecular chains, Argon [21] developed the following expression for the plastic shear strain rate, $\dot{\gamma}^p$:

$$\dot{\gamma}^p = \dot{\gamma}_0 \exp\left\{ -\frac{As_0}{T}\left[1 - \left(\frac{\tau}{s_0}\right)^{5/6}\right]\right\}. \tag{1}$$

Here, $\dot{\gamma}_0$ is a pre-exponential factor, $A$ is proportional to the activation volume/Boltzmann's constant, $T$ is the absolute temperature, $s_0 = [0.077/(1-\nu)]\mu$ is the athermal shear strength, $\mu$ is the elastic shear modulus, $\nu$ is Poisson's ratio and $\tau$ is the applied shear stress. Boyce *et al.* [15] extended this expression to include the effects of pressure and strain softening. They used $s + \alpha p$ instead of $s_0$, where $p$ is the pressure and $\alpha$ is the pressure-dependence coefficient. Further, $s$ is assumed to evolve with plastic straining via $\dot{s} = h\left(1 - \frac{s}{s_{ss}}\right)\dot{\gamma}^p$, where $h$ is the rate of resistance drop with respect to the plastic strain, and $s_{ss}$ is the assumed saturation value of $s$.

### 2.1. *Three-dimensional representation*

Consider the homogeneous deformation of a body so that its deformation gradient at a subsequent time is $\mathbf{F}$. The deformation gradient may be multiplicatively decomposed into elastic and plastic parts, $\mathbf{F} = \mathbf{F}^e\mathbf{F}^p$. Following Lee [22] and others, Boyce *et al.* [15] depart by taking $\mathbf{F}^e$ to be symmetric, so that $\mathbf{F}^p$ represents the relaxed configuration obtained by unloading without rotation (in the polar decomposition sense). Hence, $\mathbf{F}^p$ can be decomposed as $\mathbf{F}^p = \mathbf{V}^p\mathbf{R}$ with the plastic stretch $\mathbf{V}^p$ and the total stretch $\mathbf{V}$ in polar decomposition, $\mathbf{F} = \mathbf{V}\mathbf{R}$ being related by $\mathbf{V} = \mathbf{F}^e\mathbf{V}^p$. According to this decomposition, the velocity gradient is decomposed as:

$$\mathbf{L} = \dot{\mathbf{F}}\mathbf{F}^{-1} = \mathbf{D} + \mathbf{W} = \dot{\mathbf{F}}^e\mathbf{F}^{e-1} + \mathbf{F}^e\mathbf{L}^p\mathbf{F}^{e-1},$$

where $\mathbf{D}$ is the rate of deformation, $\mathbf{W}$ is the spin, and $\mathbf{L}^p = \mathbf{D}^p + \mathbf{W}^p = \dot{\mathbf{F}}^p\mathbf{F}^{p-1}$ is the velocity gradient in the relaxed configuration. With the adopted symmetry of $\mathbf{F}^e$, $\mathbf{W}^p$ is algebraically given as $\mathbf{W}$ plus a term dependent on $\mathbf{F}^e$ and $\mathbf{D} + \mathbf{D}^p$ (see Ref. [15]). Since the elastic strains will remain small, we can neglect geometry differences between current and relaxed configurations, $\mathbf{F}^e \cong \mathbf{I}$. When this approximation is carried through consistently, the constitutive equations can be simplified significantly, as discussed in Ref. [15]. In particular, it is noted that $\mathbf{W}^p \cong \mathbf{W}$ and $\mathbf{D} \cong \mathbf{D}^e + \mathbf{D}^p$, with $\mathbf{D}^e$ the symmetric part of $\dot{\mathbf{F}}^e\mathbf{F}^{e-1}$.

The rate of change of shape of the relaxed configuration, $\mathbf{D}^p$, must be constitutively prescribed. In the BPA model, the magnitude of $\mathbf{D}^p$ is taken to be given by the plastic shear strain rate, $\dot{\gamma}^p$, according to Eqn (1), while the tensor direction of $\mathbf{D}^p$ is specified by $\mathbf{N}$, so that:

$$\mathbf{D}^p = \dot{\gamma}^p\mathbf{N}, \tag{2}$$

where the direction $\mathbf{N}$ is the deviatoric part of the driving stress $\boldsymbol{\sigma}^*$ normalized by the effective equivalent shear stress $\tau$:

$$\mathbf{N} = \frac{1}{\sqrt{2}\tau}\boldsymbol{\sigma}^{*\prime}, \quad \tau = \sqrt{\frac{1}{2}\boldsymbol{\sigma}^{*\prime}:\boldsymbol{\sigma}^{*\prime}}. \tag{3}$$

The driving stress $\boldsymbol{\sigma}^*$ is itself defined by:

$$\boldsymbol{\sigma}^* = \boldsymbol{\sigma} - \mathbf{B}, \tag{4}$$

where $\boldsymbol{\sigma}$ is the Cauchy stress tensor and $\mathbf{B}$ is a back stress tensor due to strain hardening resulting from molecular alignment as will be further discussed in the next section.

In Ref. [15], the Cauchy stress is taken to be given by the elastic constitutive law [23]:

$$\boldsymbol{\sigma} = (1/J)\mathbf{L}_e:[\ln\mathbf{F}^e], \tag{5}$$

where $\mathbf{L}_e$ is the fourth-order isotropic elastic modulus tensor:

$$\mathbf{L}_e = L_e^{ijkl}\mathbf{e}_i \otimes \mathbf{e}_j \otimes \mathbf{e}_k \otimes \mathbf{e}_l,$$

$$L_e^{ijkl} = \frac{E}{2(1+\nu)}\left[(\delta^{ik}\delta^{jl} + \delta^{il}\delta^{jk}) + \frac{2\nu}{1-2\nu}\delta^{ij}\delta^{kl}\right], \tag{6}$$

with $E = 2(1+\nu)\mu$ being Young's modulus and $J = \det \mathbf{F}^e$. Although a different implementation is briefly mentioned in Ref. [15] to solve boundary value problems, we here wish to adopt a more typical viscoplastic rate formulation, as will be discussed in detail in the next section. As a consequence, we need the rate form equivalent of the elasticity Eqns (5) and (6). Since the elastic strains are assumed to remain small, we may replace the hyperelastic law (5) with the hypoelastic rate form:

$$\overset{\nabla}{\boldsymbol{\sigma}} = \mathbf{L}_e : \mathbf{D}^e, \tag{7}$$

in terms of the same modulus tensor $\mathbf{L}_e$ and employing the Jaumann stress rate $\overset{\nabla}{\boldsymbol{\sigma}} = \dot{\boldsymbol{\sigma}} - \mathbf{W}\boldsymbol{\sigma} + \boldsymbol{\sigma}\mathbf{W}$ to retain objectivity. The constitutive Eqn (7) can be finally arranged in the following form:

$$\overset{\nabla}{\boldsymbol{\sigma}} = \mathbf{L}_e : \mathbf{D} - \dot{\boldsymbol{\sigma}}_v, \tag{8}$$

where $\dot{\boldsymbol{\sigma}}_v = \mathbf{L}_e : \mathbf{D}^p$ acts as an instantaneous stress rate term that represents the viscoplastic contribution.

*2.2. Orientation hardening*

Once the material is stressed to the point of overcoming intermolecular barriers to chain motion, the molecular chains will tend to align along the direction of principal plastic stretch (e.g. Refs [20, 21]). This action decreases the configurational entropy of the system which, in turn, creates an internal network stress. This process of network distortion is very similar to that of the rubber network, and Haward and Thackray [20] suggested describing this for uniaxial extension by means of a back stress determined through a Langevin spring, as suggested by non-Gaussian network theory. Boyce *et al.* [15] extended this approach to general three-dimensional plastic deformations by introducing a back stress tensor $\mathbf{B}$ which is taken to be coaxial with the plastic stretch tensor $\mathbf{V}^p$. Thus, if $\mathbf{e}_i^p$ are the unit eigenvectors of $\mathbf{V}^p$, corresponding to a plastic stretch $\lambda_i^p$, then the back stress $\mathbf{B}$ is constructed as:

$$\mathbf{B} = \sum_i B_i(\mathbf{e}_i^p \otimes \mathbf{e}_i^p)$$

from the principal components $B_i$. Originally, they adopted the classical so-called three-chain model, for which the principal components $B_i^{3-ch}$ of the back stress tensor are given in terms of the plastic stretches $\lambda_i^p$ by (see e.g. Ref. [24]):

$$B_i^{3-ch} = \frac{1}{3}C^R\sqrt{N}\left[\lambda_i^p\,\mathscr{L}^{-1}\left(\frac{\lambda_i^p}{\sqrt{N}}\right) - \frac{1}{3}\sum_{j=1}^{3}\lambda_j^p\,\mathscr{L}^{-1}\left(\frac{\lambda_j^p}{\sqrt{N}}\right)\right]. \tag{9}$$

Here, $C^R$ is known as the rubbery modulus, $N$ is a statistical network parameter related to the network locking stretch and $\mathscr{L}$ is the Langevin function defined by $\mathscr{L}(\beta) = \coth\beta - 1/\beta$.

However, very recently, Arruda and Boyce [16, 17] found that the three-chain non-Gaussian network model was not capable of picking up the strain hardening observed experimentally in PC and PMMA. At the same time, they suggested modelling the network by eight equivalent chains instead of three, and obtained closer agreement with their experimental results for PC and PMMA. The principal components of the back stress tensor according to this eight-chain non-Gaussian network model are:

$$B_i^{8-ch} = \frac{1}{3}C^R\sqrt{N}\,\frac{\lambda_i^{p2} - \lambda^{p2}}{\lambda^p}\,\mathscr{L}^{-1}\left(\frac{\lambda^p}{\sqrt{N}}\right), \quad \lambda^{p2} = \frac{1}{3}\sum_{j=1}^{3}\lambda_j^{p2}. \tag{10}$$

Both the three-chain and eight-chain models are based on approximate representations of the actual spatial distributions of molecular chains by "lumping" them in three and eight specific directions, respectively. Very recently, the authors developed the so-called full

network model in which full account is taken of the orientation distribution of the individual chains in the network [18]. This model is a three-dimensional generalization for arbitrary deformation paths of the two-dimensional model for proportional deformations proposed by Treloar and Riding [25]. The principal back stresses according to this model can be given in two equivalent ways, depending on whether one considers the chain orientation distribution in the undeformed isotropic or in the current deformed state; here, we only reiterate the expression according to the first point of view, because it is more convenient for applications:

$$B_i = \frac{1}{4\pi} C^R \sqrt{N} \int_0^{\pi} \int_0^{2\pi} \mathscr{L}^{-1}\left(\frac{\lambda^p}{\sqrt{N}}\right) \frac{\lambda_i^{p2}(m_i^0)^2 - \frac{1}{3}\lambda^{p2}}{\lambda^p} \sin\theta_0 \, d\theta_0 \, d\varphi_0, \quad \lambda^{p2} = \sum_i (m_i^0)^2 \lambda_i^{p2}. \tag{11}$$

Here, the $m_i^0$ are the components of the unit vector $\mathbf{m}^0$ in the orientation space $(\theta_0, \varphi_0)$ defined by:

$$m_1^0 = \sin\theta_0 \cos\varphi_0, \quad m_2^0 = \sin\theta_0 \sin\varphi_0, \quad m_3^0 = \cos\theta_0,$$

where $\theta_0$ and $\varphi_0$ measure the orientation of molecular chains relative to the principal stretch directions in the undeformed configuration. Furthermore, an accurate approximation of the full network predictions according to Eqn (11) has been found [18] in the form of a combination of the three-chain and eight-chain model predictions, Eqns (9) and (10), through:

$$B_i = (1 - \rho_p) B_i^{3\text{-ch}} + \rho_p B_i^{8\text{-ch}}, \tag{12}$$

thus avoiding the rather time-consuming integration procedure involved in Eqn (11). Here, $\rho_p$ is defined as being related to the maximal principal plastic stretch $\lambda_{max}^p = \max(\lambda_1^p, \lambda_2^p, \lambda_3^p)$ via $\rho_p = 0.85\lambda_{max}^p/\sqrt{N}$. All computations employing the full network model to be reported here have used the expression (12).

## 3. PROBLEM FORMULATION AND METHOD OF SOLUTION

We consider a uniform circular cylindrical tube of initial outer radius $R_{oo}$ initial inner radius $R_{io}$, and initial length $L_0$, which is subjected to a twist $\varphi$ due to an applied torque $M$. Also, the bar may be subjected simultaneously to an axial force $F$ associated with an axial displacement $U$. The end faces of the bar are constrained such that they remain plane and perpendicular to the axial direction, and it is assumed, in fact, that any cross-section of the bar remains plane. The lateral surfaces of the bar are traction-free and all properties are assumed to be axisymmetric and homogeneous along the axial direction. Although deformation-induced anisotropy may occur, the behaviour remains axisymmetric and is further assumed to remain uniform in the axial direction. Thus, we neglect the formation and propagation of macroscopic circumferential shear bands that may develop (see e.g. Refs [13, 29]). Consequently, the bar remains circular cylindrical, and at the current deformed state has an outer radius $R_o$, an inner radius $R_i$, and a length $L$. This problem and the adopted numerical method are a natural extension of the solid bar problem studied in Refs [3–5] within the context of metal plasticity. In the sequel we give a brief, but complete, summary of the governing equations.

All governing equations will be referred to a spatially fixed cylindrical coordinate system $x^i = (r, \theta, z)$ with orthonormal base vectors $\mathbf{e}_i$. These base vectors are associated with the current state, so that the various tensor components to be used in the sequel represent the respective physical components. However, due account must be given to the fact that the base vectors are spatially fixed so that their material time derivative will generally not vanish since the coordinate system is curvilinear (see Ref. [26]).

The kinematics of the problem are readily established. The deformations are such that if the initial coordinates of a material point are $x_0^i = (r_0, \theta_0, z_0)$, its current coordinates are $x^i = (r, \theta, z)$, where:

$$r = r(r_0; t), \quad \theta = \theta_0 + \psi(t) z_0, \quad z = e(t) z_0, \tag{13}$$

with $t$ being time. Here, $\psi = \varphi/L_0$ represents the twist per unit length of the bar in the initial

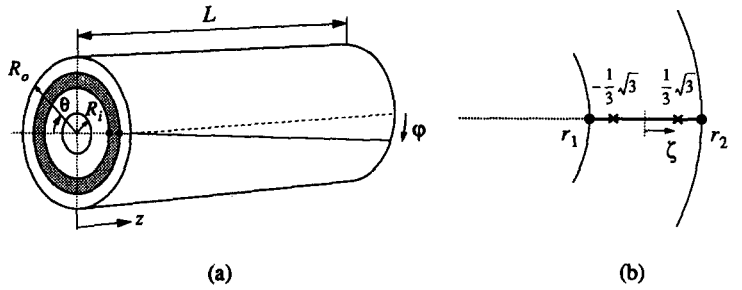


FIG. 1. The finite elements used here are cylindrical tubes with inner radius $r_1$ and outer radius $r_2$: (a) definition of nodal points (●); and (b) material sampling points (×).

configuration and $e = L/L_0 = 1 + U/L_0$ is the extensional stretch in the axial direction. The components of the velocity vector $\mathbf{v} = v_i\mathbf{e}_i$ are given by $(v_i) = (\dot{r}, z\dot{\psi}/e, z\dot{e}/e)$ and the components of $\mathbf{D} = D_{ij}\mathbf{e}_i \otimes \mathbf{e}_j$ and $\mathbf{W} = W_{ij}\mathbf{e}_i \otimes \mathbf{e}_j$ are found to be given by:

$$D_{11} = \frac{\partial \dot{r}}{\partial r}, \quad D_{22} = \dot{r}/r, \quad D_{33} = \frac{\dot{e}}{e}, \quad D_{23} = \frac{1}{2}r\frac{\dot{\psi}}{e}, \quad D_{12} = D_{13} = 0; \tag{14a}$$

$$W_{12} = -z\frac{\dot{\psi}}{e}, \quad W_{13} = 0, \quad W_{23} = \frac{1}{2}r\frac{\dot{\psi}}{e}. \tag{14b}$$

Regarding the stress state inside the bar, axisymmetry and axial homogeneity imply that the components of Cauchy stress $\boldsymbol{\sigma} = \sigma_{ij}\mathbf{e}_i \otimes \mathbf{e}_j$ satisfy $\sigma_{12} = \sigma_{13} = 0$, while $\sigma_{ij} = \sigma_{ij}(r; t)$ otherwise. The resultant torque, $M$, and axial tensile force, $F$, are given by:

$$M = 2\pi\int_{R_i}^{R_o} r^2\sigma_{23}\mathrm{d}r, \quad F = 2\pi\int_{R_i}^{R_o} r\sigma_{33}\mathrm{d}r, \tag{15}$$

while the lateral surfaces are traction-free, $\sigma_{11}(R_i) = 0$ and $\sigma_{11}(R_o) = 0$. Free-end torsion is analysed by specifying the boundary condition $F = 0$, while fixed-end torsion follows from the condition $\dot{e} = 0$.

It is observed that for the present axisymmetric problem, the pertinent quantities depend only on the radial coordinate $r$. This problem can be dealt with in an efficient way by means of special purpose finite elements in the radial direction as demonstrated in Ref. [3]. As shown schematically in Fig. 1a, the elements used are circular cylindrical tubes, with inner radius $r_1$ and outer radius $r_2$ in the current configuration. Such an element is geometrically one-dimensional along the $r$-axis, with two nodes at $r = r_1$ and $r = r_2$, respectively (see Fig. 1b). In addition to the overall axial displacement $U$ and the angle of twist $\varphi$, the degrees of freedom of the element are the radial nodal displacements. It is numerically convenient to take the element's vector v of degrees of freedom as:

$$\mathrm{v} = \left[\frac{\dot{r}_1}{r_1}\ \frac{\dot{r}_2}{r_2}\ \frac{\dot{\psi}}{e}L\ \frac{\dot{e}}{e}\right]^T, \tag{16}$$

in terms of the radial nodal velocities $\dot{r}_1$ and $\dot{r}_2$. The radial velocity at any radius within the element is determined by assuming a linear interpolation of $\dot{r}/r$ between the nodal values. The element's force vector F dual to v, such that $\mathrm{F}^T\mathrm{v}$ is the rate of work of the loads on the element, is then given by:

$$\mathrm{F} = [r_1F_{r1}\ \ r_2F_{r2}\ \ M^l\ \ LF^l]^T, \tag{17}$$

where $F_{r1}$ and $F_{r2}$ are the radial forces on the inner and outer surfaces of the element, respectively, and where $M^l$ and $F^l$ are the torque and the axial force, respectively, that act on the element. The total torque $M$ and the total axial force $F$ acting on the bar obtained by summation over all elements: $M = \sum_l M^l$, $F = \sum_l F^l$.

The governing FE equations are formulated within a framework using the concept of material sampling points and this leads to element equilibrium equations of the form:

$$\mathrm{D}^T\Sigma = \mathrm{F}, \tag{18}$$

where $\Sigma$ is a vector containing the sampling point stress components and D is a matrix depending on the current geometry (see Appendix). Since the lateral surfaces of the bar are traction-free, not only must all internal nodal radial forces $F_{ri}$ vanish, but also the radial force at the outmost node at $r = R_o$ and at the innermost node $r = R_i$. The rate equilibrium conditions at the current instant are obtained by straightforward time differentiation. After elimination of the stress rates by means of the constitutive Eqn (8), the following finite element equations for the unknown v are obtained:

$$\mathrm{K}\mathrm{v} = \dot{\mathrm{F}} + \dot{\mathrm{F}}_{\mathrm{v}}$$

(see Appendix). Here $\dot{\mathrm{F}}_{\mathrm{v}}$ acts as an additional force rate that represents the viscous terms and is calculated from $\boldsymbol{\sigma}_{\mathrm{v}}$ appearing in Eqn (8).

The deformation process is then analysed employing a linear incremental solution procedure, based on a time step $\Delta t$, with simultaneous updating of the configuration. At each increment, the twisting increment $\Delta\psi = \dot{\psi}\Delta t$ and the stretching increment $\Delta e = \dot{e}\Delta t$, as well as the nodal radial displacement increments, are obtained from the equations:

$$\mathrm{K}(\Delta t\,\mathrm{v}) = \Delta t(\dot{\mathrm{F}} + \dot{\mathrm{F}}_{\mathrm{v}}) - (\mathrm{D}^{\mathrm{T}}\Sigma - \mathrm{F}), \tag{19}$$

assembled for the entire bar. The equilibrium conditions (18) are included in the right-hand side in order to prevent drifting of the solution away from the true equilibrium path. Finally, the increments of the sampling point stresses are evaluated by $\Delta\boldsymbol{\sigma} = \dot{\boldsymbol{\sigma}}\Delta t$ and similarly for the other pertinent quantities, except for the back stress **B** which can be computed from the current plastic state of deformation instantaneously.

## 4. RESULTS

The torsion problem described in Section 3 involves a number of nondimensional groups, and therefore we introduce the following quantities:

$$\Gamma = \varphi\frac{R_{o0}}{L_0}, \quad \bar{\tau} = \frac{3M}{2\pi(R_{o0}^3 - R_{i0}^3)s_0}, \quad \bar{\sigma} = \frac{F}{\pi(R_{o0}^2 - R_{i0}^2)s_0}. \tag{20}$$

These quantities, along with the overall axial logarithmic strain $\varepsilon = \ln e$ can be used to efficiently present the overall response of the specimen, irrespective of its exact geometry. To enable a direct comparison with experimental data for PC from Ref. [13] we have taken the actual dimensions to be the same as in Ref. [13], i.e. $R_{o0} = 3.175$ mm and $L_0 = 6.35$ mm, while the initial inner radius is $R_{i0} = 1.5875$ mm for the tube. All numerical calculations were carried out at a constant twist rate $\dot{\varphi} = 0.02\ \mathrm{rad\,s^{-1}}$ corresponding to a shear rate $\dot{\Gamma} = 0.01\,\mathrm{s}^{-1}$.

At room temperature ($T = 294$K), the following values of the parameters that determine the strain rate, temperature dependence and softening behaviour for PC are used: $\dot{\gamma}_0 = 2\times10^{15}\,\mathrm{s}^{-1}$, $A = 240\,\mathrm{K\,MPa}^{-1}$, $s_0 = 111$ MPa, $s_{ss}/s_0 = 0.92$, $h = 500$ MPa and $\alpha = 0.08$, while Young's modulus and Poisson's ratio are taken as $E = 2623$ MPa and $\nu = 0.3$, respectively. Most of this data has been taken from tensile experiments reported in Ref. [27]; however, the value of the shear strength has been fitted with the yield point observed in the torsion experiments [13], while the saturation value $s_{ss}$ has been chosen to fit the softening behaviour observed during simple shear of PC by G'Sell [28]. The parameters $C^{\mathrm{R}}$ and $N$ that govern the orientational hardening are taken as $C^{\mathrm{R}} = 3.7$ MPa and $N \approx 6$ (see Reference 27 in Ref. [28]). Admittedly, the material parameters have been compiled from different sources involving different experiments on material that is unlikely to be exactly the same, but because of the lack of sufficient experimental data, this was the best we could do. In any case, with the exception of the yield point, the torsion results to be presented here provide an independent comparison with the experiments in Ref. [13].

In Ref. [3], the predicted stress distributions for an incompressible elastic solid bar in fixed-end torsion were compared with the analytical solution available when the torsion angle is small. Even with only five elements, the stress distribution was represented with sufficient accuracy. In Ref. [4] further checks were performed for an incompressible elasto-plastic material by comparison with highly accurate results from a semi-analytical method,

and again it was found that sufficiently accurate results were obtained by using only five elements. However, for a tube, one cannot expect to get highly accurate results using only five elements, because of the intrinsic properties of the special element and the additional lateral inner boundary condition $\sigma_{11}(R_i) = 0$ involved. In order to obtain sufficiently accurate results, we use a somewhat refined mesh near the lateral surfaces (especially near the inner surface) where high strain gradients are expected. Numerical experiments show for a tube that the computed torque and axial force, as well as the shear stress distributions, are not sensitive to the number of elements; however, the second-order effects, such as the radial stress distribution, are indeed rather sensitive to the number of elements used. Figure 2 shows a typical stress distribution for a twist corresponding to $\Gamma = 2$, using three different meshes consisting of five equally sized elements, 100 elements or 15 elements with a local refinement as shown in Fig. 3 (the stress distributions are plotted by linear interpolation between sampling point values). Clearly, the differences in predicted shear stress are very small, but the radial stress distribution near the inner radius with a uniform mesh comprising only five elements is very poor. Since this paper primarily focusses on the overall characteristics of torsion (torque, axial force, elongation, etc.) which are not very sensitive to deviations from the actual stress state, it was decided that the mesh shown in Fig. 3 for the tube would be sufficiently accurate. A similar mesh is used for the solid bar.

### 4.1. *Fixed-end torsion*

We first study the fixed-end torsion of PC specimens. This corresponds to invoking the axial boundary conditions $\dot{e} = \dot{U} = 0$ and will lead to the development of an axial force $F$.

Figure 4 shows the torque responses to fixed-end torsion of the tube and of the solid bar in terms of the torque $M$ and the twist $\varphi$. Later, the torque responses are plotted in terms of the nondimensional torque $\bar{\tau}$ and the shear strain $\Gamma$ defined in Eqn (20). It is found that the overall trends obtained for the torque fixed-end torsion is similar to the evolution of the shear stress in simple shear as studied e.g. in Ref. [19]. The response is characterized by: (i) an initially elastic response which ends at the yield point when the torsion angle $\varphi$ is about 0.3 rad ($\Gamma \approx 0.15$); (ii) a small but significant torque drop after plastic deformation has been initiated, which at the current levels of strain must be attributed to the material softening; and (iii) a gradual hardening starting around $\varphi \approx 2$ rad ($\Gamma \approx 1$) and which ends when the

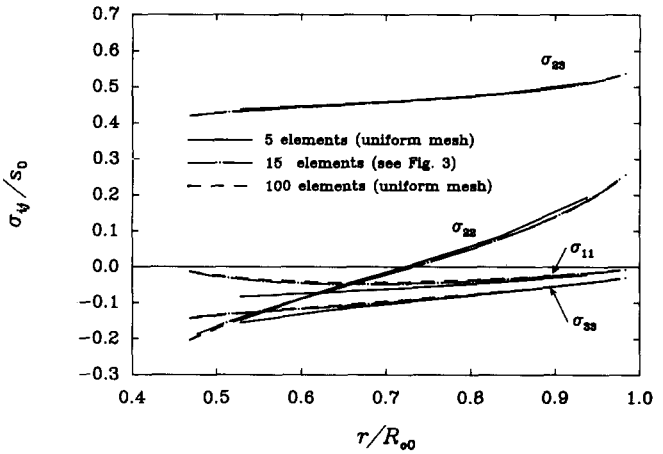


FIG. 2. Stress distributions inside the tube in fixed-end torsion for $\Gamma = 2$ using different meshes (note the reduction of the radii of the tube; see also Fig. 5).


FIG. 3. The finite element mesh used for the tube comprising 15 elements.

maximum plastic stretch at the outer radius approaches the locking stretch $N^{1/2}$ of the macromolecular chain network. Also shown are a number of experimental points taken from Ref. [13]. It is found that the constitutive model, together with the numerical tool used here, is capable of capturing a number of major characteristics of the plastic torsion behaviour in a qualitatively reasonable way. The small-strain viscoelastic effect observed in the experiments, as indicated by the deviation from the linear elastic response prior to yield, is not accounted for in the constitutive model.

Although axial loads were not monitored during their experiments, Wu and Turner [13] stated that no axial force is expected during twisting of a tube made from an isotropic material if it does not undergo a volume change; if the material tends to change its volume an axial force may develop. Before presenting the axial loads found in our simulations, we first consider the volume changes predicted here. Figure 5 presents the evolution of the outer radius $R_o$ and inner radius $R_i$ during torsion of the tube. It is clear that both $R_o$ and $R_i$ decrease monotonically while the length of the specimen is kept fixed. It is also found from Fig. 5 that the thickness of the tube slowly increases. At the maximum twist, $\Gamma = 2.2$, the wall thickness has changed by about 4%, corresponding to a reduction in volume of the tube of only about 0.2%. It is emphasized that according to the constitutive model of Section 2, this volume reduction is entirely due to elastic deformations.

The predicted axial forces for the tube and for the solid bar are presented in Fig. 6. It is found that, in terms of the dimensionless force $\bar{\sigma}$, the tube and the solid bar exhibit a similar

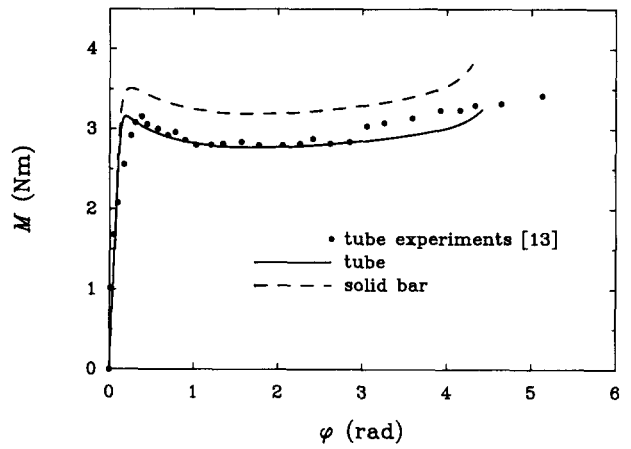


FIG. 4. Torque responses in fixed-end torsion for the solid bar ($R_i = 0$) and for the tube ($R_{io}/R_{oo} = 0.5$). The experimental data for the tube are taken from Ref. [13].

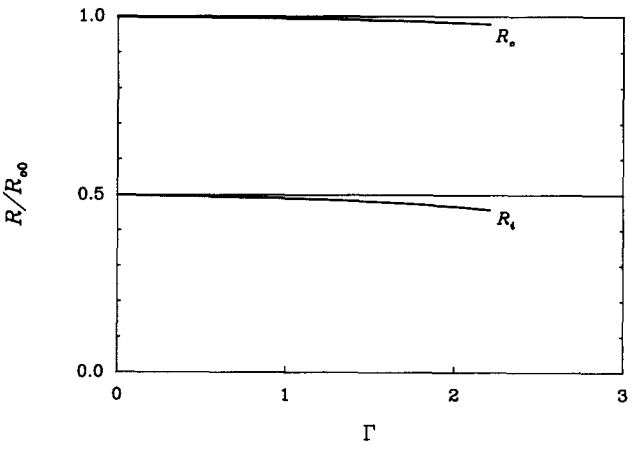


FIG. 5. Evolution of the outer radius $R_o$ and the inner radius $R_i$ during fixed-end torsion.

axial response. The prime characteristic of the response is that the axial force developed during twisting is compressive. There appears to be a rapid initiation during the first elastic stage of the deformation, followed by a stage of little change after yielding and softening, while the axial force increases rapidly again during the strain-hardening stage. The value of the axial force attained prior to yielding is consistent with the dilatation of 0.2% mentioned above. In the model used here, volume changes are attributed to elastic deformations only, and with a value of the bulk modulus of $B = E/[3(1 - 2\nu)] = 2186$ MPa, the compressive axial load agrees with that shown in Fig. 6. Obviously, this argument cannot explain the subsequent three-fold increase with ongoing plastic deformation. The latter phenomenon must be attributed to the deformation-induced anisotropy associated with the deformation of the entangled molecular network in glassy polymers.

As has been demonstrated in Fig. 2, the stress distributions in the tube or solid bar are quite nonuniform. For practical purposes, it may be of interest however to have an approximate tool to link the twisting of a tube or solid bar to homogeneous simple shear. If the shear stress distribution is approximated to be constant across the entire cross-section, then this shear stress is readily found to be related to the applied torque $M$ through the quantity $\bar{\tau}s_0$ defined in Eqn (20). To assess the accuracy of this approximation, we replot in Fig. 7 the torque responses found for the tube and solid bar in comparison with the shear stress response to homogeneous simple shear to a shear strain $\Gamma$ obtained by direct straightforward integration of the constitutive equations (see Ref. [19]). It is seen that the

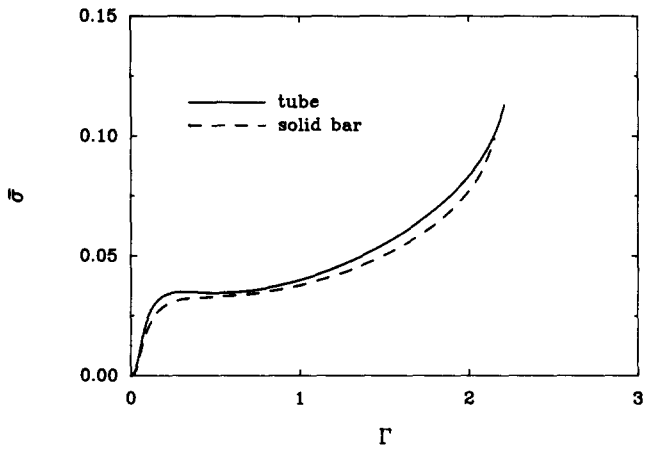


FIG. 6. Development of compressive axial forces in fixed-end torsion.

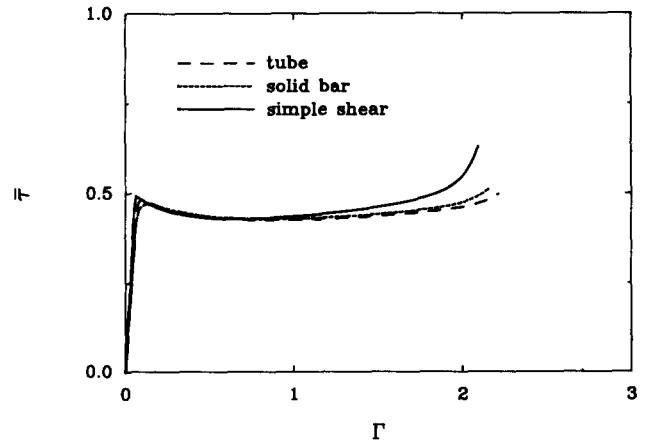


FIG. 7. Normalized torque responses to fixed-end torsion in comparison with the shear stress responses to homogeneous simple shear.

simple representation in terms of $\bar{\tau}$ gives a reasonable estimate of the simple shear behaviour up to moderately large strains of the order of 1, but that at larger strains the stress inhomogeneity in the actual specimen becomes too large to give an adequate agreement.

To assess the difference between the behaviour of the tube and the solid bar, we present the stress distributions across the solid bar when $\Gamma = 2$ in Fig. 8. Comparing with the results for the tube shown in Fig. 2, the shear stress in the tube is much more uniform than in the solid bar. The reason is that in the solid bar, the material close to the axis of the bar remains in the small deformation state up to the moment that the maximum plastic stretch at the outer surface approaches the limit stretch of the network.

Reducing the wall thickness of a tube will reduce the nonuniformity of the deformation. In fact, many experimental procedures based on torsion have used thin-walled specimens for which the state of deformation has been assumed to be completely uniform and, for fixed-end torsion, to be a state of simple shear (see e.g. Ref. [11]). In order to check this hypothesis, we present the stress distributions in such a tube with $R_{i0} = 19/20R_{o0}$ in fixed-end torsion in Fig. 9. It is observed that the shear stress, the axial normal stress and radial normal stress are indeed uniform across the wall thickness with fair accuracy, but the hoop stress still exhibits a significant variation.

### 4.2. *Free-end torsion*

We proceed by studying the torsion of the same tube and the same solid bar as in the previous subsection, but under conditions of axially free ends. These conditions are

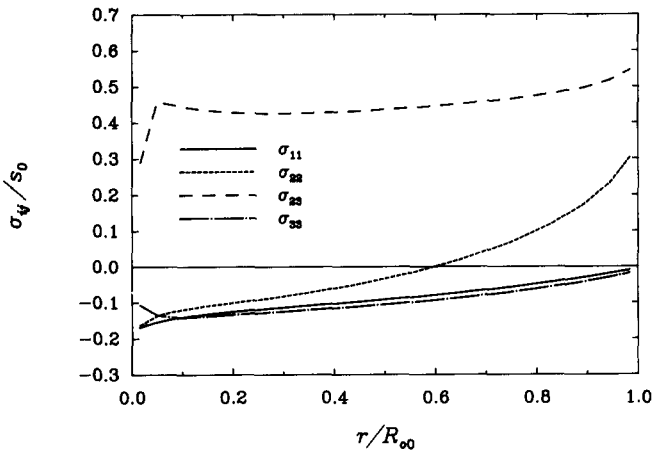


FIG. 8. Stress distributions in the solid bar in fixed-end torsion at $\Gamma = 2$.

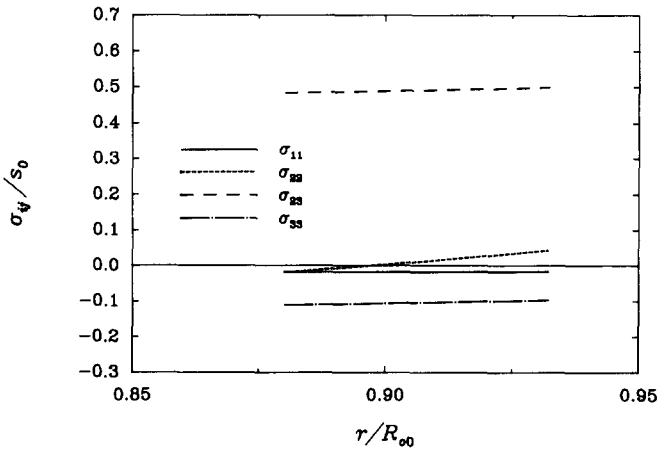


FIG. 9. Stress distributions in a thin-walled tube ($R_{i0}/R_{o0} = 19/20$) in fixed-end torsion at $\Gamma = 2$.

obtained by imposing the opposite axial boundary condition to that in the previous case of fixed-end torsion, i.e. $F = 0$ in Eqn (16), thus allowing for an axial elongation $e$.

Figures 10 and 11 present the torque responses and the accompanying axial elongation development in the tube and in the solid bar during free-end torsion. The difference between the tube and the solid bar in predicted torque is similar to that in fixed-end torsion. The torque responses found during free-end torsion differ rather little from those found in fixed-end torsion (Fig. 4); careful inspection shows that the free-end tests exhibit less strain hardening at the final stages of deformation.

Figure 11 shows that the axial strains that develop during free-end twisting may attain quite significant values of up to 6%. The axial strain is found to increase almost linearly up to $\Gamma \approx 1$ while growing increasingly fast for larger twists. Figure 11 also shows a significant difference in elongation between the tubular and the solid specimen. Furthermore, it is interesting to note that the axial strain develops in a distinctly different manner from the axial forces during fixed-end torsion (Fig. 6), and does not display a long-range plateau of very small apparent slope. Nevertheless, both second-order effects are attributed to the same feature of the material's response, namely deformation-induced anisotropy.

Wang *et al.* [29] give some experimental results for free-end torsion of solid specimens made of various types of polymers, including a PC. Their torque response is qualitatively similar to that shown in Fig. 10, albeit the maximum shear strain attained in their experiments was only about 0.4, i.e. well in the softening regime. The particular type of PC

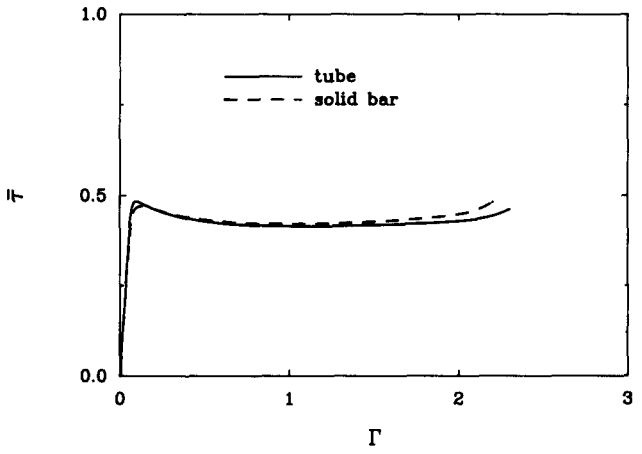


FIG. 10. Torque responses in free-end torsion for the solid bar ($R_i = 0$) and for the tube ($R_{io}/R_{oo} = 0.5$).

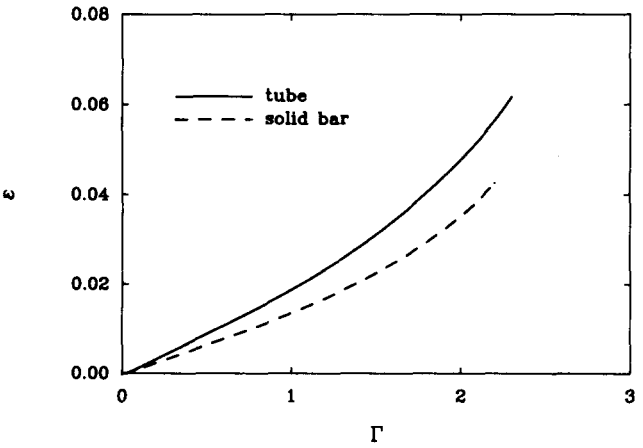


FIG. 11. Axial elongations in free-end torsion of tube or solid bar.

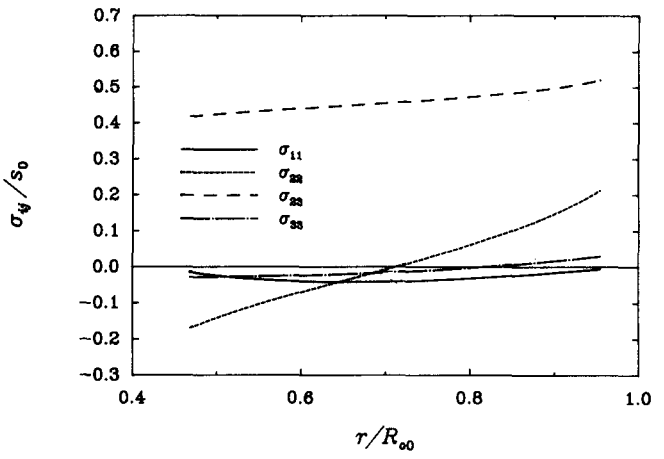


FIG. 12. Stress distributions in the tube in free-end torsion at $\Gamma = 2$.

used in those experiments is rather different from that assumed in the computations: the value of $s_0$ estimated from the torque at yield is only about 90 MPa. Data for elongation and volume changes are only given in Ref. [29] up to yield, and thus represent only the elastic behaviour.

The predicted stress distributions across the tube are shown in Fig. 12.

## 5. CONCLUSION

In this paper, we have analysed the large-strain elastic–viscoplastic torsion of circular cylindrical tubes and solid bars under fixed-end, as well as free-end conditions, using a numerical method based on simple, special purpose finite elements.

The predicted response of a tube under fixed-end torsion has been compared with available experimental data for polycarbonate, based on material properties taken (with one exception) from independent sources. The calculation stopped at $\Gamma = 2.2$ when the maximum plastic stretch approached the locking stretch of the macromolecular chain network. Generally speaking, the agreement is reasonable, even though our simulations cannot reflect the initiation and propagation of macroscopic shear bands observed experimentally. Preliminary numerical studies of shear band propagation in simple shear with the same constitutive model [30] seem to support the approximation involved: the results suggest that the torque response during propagation is affected only slightly, while the response after propagation is completed is identical to that which occurs when the deformation is presumed to remain uniform during the entire process. A number of features in the experimental results are not picked up by the constitutive model. We shall return to this later.

As expected, stress distributions in a tube are more homogeneous than in a solid bar (see Figs 2 and 8). For the tube considered here, the variations through the thickness of the tube are small for the shear stress, but can be large for the other stress components. It has been verified that if the tubes are very thin, then the deformation can be approximated as being homogeneous with fair accuracy and experimental results for torsion can be easily interpreted; however, such a specimen is known to be unstable at large strains (torsional buckling is a primary mode of failure for such a specimen). On the other hand, the numerical method developed here is capable of simulating large-strain torsion of tubes with any values of $R_{i0}$ ($0 \leqslant R_{i0}/R_{o0} < 1$). Furthermore, it is fairly easy to incorporate other viscoplastic constitutive models into this special finite element program. Therefore, it provides a useful tool to interpret experimental torsion results on thick-walled tubes or solid specimens, and thus to determine the material parameters appearing in the constitutive models.

The axial force in fixed-end torsion and the axial elongation in free-end torsion are mainly due to the development and the subsequent rotation of the induced anisotropy. For

the amorphous polymers considered here, the anisotropy is associated with the stretching of the entangled molecular chain structure. It is well known that the prediction of such second-order phenomena generally shows a rather strong dependence on the constitutive models—in particular the description of anisotropic hardening. For large-strain torsion of a solid bar of polycarbonate, this has been studied in Ref. [14] by considering, in addition to the full network model, the simplified three- and eight-chain models. It is observed in Ref. [14] that all three orientation hardening models discussed in Section 2 give virtually identical axial force predictions up to $\Gamma \approx 1$. For large twists, the three-chain model predicts very large compressive axial forces, but when using the eight-chain model, the magnitude of the axial force reduces drastically. The axial force predicted by the full network model is in between that predicted by the three-chain model and eight-chain model, respectively. Similar phenomena have been observed for the predicted axial elongations during free-end torsion. Unfortunately, we have not been able to find any experimental data on axial force or elongation development during torsion of PC in order to compare these predicted results with experiments (Ref. [29] only gives such data prior to yield).

One of the most important differences between simulated and experimental response to fixed-end torsion is that our simulations tend to overestimate the strain hardening at large plastic strains. This is intimately connected with the affine network theory used here to model orientational hardening. As discussed in some detail in Ref. [19], the idea of using an affine network theory to model the stretching of the molecular network assumes that the junction points in the network remain intact. However, it has been suggested in the literature (see e.g. Ref. [31] and [32]) that physical entanglements in amorphous polymers are being pulled out during deformation. In terms of our network model, this would mean that the number of chains $n$ reduces in the course of the deformation process, while the number of links $N$ per chain increases, thus reducing the stiffness of the network.

Furthermore, especially the axial effects predicted here may depend sensitively on the particular way of incorporating deformation-induced anisotropy by means of the effective stress concept in Eqn (3). This is likely to be rather important in the above torsional problem, where the stress history is nonproportional and significant rotations of the principal axes occur. A totally different approach to modelling orientational hardening has been adopted in Ref. [33]. All these constitutive aspects require further study. The formulation of improved models and their implications for large-strain torsion are in progress and will be reported elsewhere.

## REFERENCES


1. K. W. Neale and S. C. Shrivastava, Finite elastic–plastic torsion of a circular bar. *Engng Fracture Mech.* **21**, 747 (1985).
2. K. W. Neale and S. C. Shrivastava, Kinematic work hardening models and their implications for large strain plastic behaviour in torsion. In *Yielding, Damage and Failure of Anisotropic Solids* (edited by J. P. Boehler), p. 131. Mechanical Engineering Publications, London (1990).
3. P. D. Wu and E. van der Giessen, Analysis of elastic–plastic torsion of circular bars at large strains. *Arch. Appl. Mech.* **61**, 89 (1991).
4. E. van der Giessen, P. D. Wu and K. W. Neale, On the effect of plastic spin on large elastic–plastic torsion of solid bars. *Int. J. Plasticity* **8**, 773 (1992).
5. E. van der Giessen, P. D. Wu and K. W. Neale, Effect of plastic spin and deformation-induced anisotropy on large strain torsion of solid bars. In *Constitutive Relations for Finite Deformation of Polycrystalline Metals* (edited by R. Wang and D. C. Drucker), p. 233. Springer, Beijing/Berlin (1992).
6. W. Swift, Length changes in metals under torsional overstrain. *Engineering* **163**, 253 (1947).
7. J. A. Bailey, S. L. Haas and K. C. Nawab, Anisotropy in plastic torsion. *J. Basic Engng* **94**, 231 (1972).
8. E. W. Billington, Non-linear response of various metals: II. Permanent length changes in twisted tubes. *J. Phys. D: Appl. Phys.* **10**, 533 (1977).
9. J. Gil-Sevillano, P. Van Houtte and E. Aernoudt, Deutung der schertexturen mit hilfe der Taylor-analyse. *Z. Metallkunde* **66**, 367 (1975).
10. S. Harren, T. C. Lowe, R. J. Asaro and N. Needleman, Analysis of large-strain shear rate-dependent face-centered cubic polycrystals: correlation of micro- and macromechanics. *Phil. Trans. R. Soc. Lond.* **A328**, 443 (1989).
11. C. S. White, C. A. Bronkhorst and L. Anand, An improved isotropic–kinematic hardening model for moderate deformation metal plasticity. *Mech. Mater.* **10**, 127 (1990).

12. R. KHEN and M. B. RUBIN, Analytical modelling of second order effects in large deformation plasticity. *Int. J. Solids Structures* **29**, 2235 (1992).
13. W. WU and A. P. L. TURNER, Shear bands in polycarbonate. *J. Polym. Sci.: Polym. Phys. Edition* **11**, 2199 (1973).
14. P. D. WU and E. VAN DER GIESSEN, Large strain visco-plastic torsion of circular bars of glassy polymers, in *Advances in Engineering Plasticity and its Applications* (edited by W. B. LEE), p. 477. Elsevier, Amsterdam (1993).
15. M. C. BOYCE, D. M. PARKS and A. S. ARGON, Large inelastic deformation of glassy polymers, Part I: rate dependent constitutive model. *Mech. Mater.* **7**, 15 (1988).
16. E. M. ARRUDA and M. C. BOYCE, Evolution of plastic anisotropic in amorphous polymers during finite straining, in *Anisotropy and Localization of Plastic Deformation* (edited by J. P. BOEHLER and A. S. KHAN), p. 483. Elsevier, London (1991).
17. E. M. ARRUDA and M. C. BOYCE, Evolution of plastic anisotropic in amorphous polymers during finite straining. *Int. J. Plasticity* (in press).
18. P. D. WU and E. VAN DER GIESSEN, On improved 3-D non-Gaussian network models for rubber elasticity. *Mech. Res. Comm.* **19**, 427 (1992).
19. P. D. WU and E. VAN DER GIESSEN, On improved network models for rubber elasticity and their applications to orientation hardening in glassy polymers. *J. Mech. Phys. Solids* **41**, 427 (1993).
20. R. N. HAWARD and G. THACKRAY, The use of mathematical model to describe isothermal stress–strain curves in glassy thermoplastics. *Proc. R. Soc. Lond.* **A302**, 453 (1968).
21. A. S. ARGON, A theory for the low-temperature plastic deformation of glassy polymers. *Phil. Mag.* **28**, 839 (1973).
22. E. H. LEE, Elastic–plastic deformation at finite strains. *J. Appl. Mech.* **36**, 1 (1969).
23. L. ANAND, On H. Hencky's approximate strain-energy function for moderate deformation. *J. Appl. Mech.* **46**, 78 (1979).
24. M. C. WANG and E. GUTH, Statistical theory of networks of non-Gaussian flexible chains. *J. Chem. Phys.* **20**, 1144 (1952).
25. L. R. G. TRELOAR and G. RIDING, A non-linear theory for rubber in biaxial strain. I. Mechanical properties. *Proc. R. Soc. Lond.* **A369**, 261 (1979).
26. E. VAN DER GIESSEN, Some remarks on the analysis of large strain torsion-like problems. *Acta Mech.* **89**, 233 (1991).
27. M. C. BOYCE and E. M. ARRUDA, An experimental and analytical investigation of large strain compressive and tensile response of glassy polymers. *Polym. Engng Sci.* **30**, 1288 (1990).
28. C. G'SELL, Plastic deformation of glassy polymers: constitutive equations and macromolecular mechanisms, in *Strength of Metals and Alloys* (edited by H. J. MCQUEEN, J. P. BAILON, J. I. DICKSON, J. J. JONAS and M. G. AKBEN), p. 1943. Pergamon Press, Oxford (1986).
29. T. T. WANG, H. M. ZUPKO, L. A. WYNDON and S. MATSUOKO, Dimensional and volumetric changes in cylindrical rods of polymers subjected to a twist moment. *Polymer* **23**, 1407 (1982).
30. P. D. WU and E. VAN DER GIESSEN, A modified 3-D constitutive model for glassy polymers and its application to large simple shear of polycarbonate, in *Modelling of Plastic Deformation and its Engineeering Applications* (edited by S. I. ANDERSEN *et al.*), p. 519. Roskilde, Denmark (1992).
31. S. RAHA and P. B. BOWDEN, Birefringence of plastically deformed poly(methyl methacrylate). *Polymer* **13**, 174 (1972).
32. P. A. BOTTO, R. A. DUCKETT and I. M. WARD, The yield and thermoelastic properties of oriented poly(methyl methacrylate). *Polymer* **28**, 257 (1987).
33. S. D. BATTERMAN and J. L. BASSANI, Yielding, anisotropy and deformation processing of polymers. *Polym. Engng Sci.* **30**, 1281 (1990).
34. E. VAN DER GIESSEN, FE-thermomechanics and material sampling points. *Comput. Meth. Appl. Mech. Engng* **64**, 447 (1987).

## APPENDIX

Here we give a brief summary of the central governing equations of the special element used in the analysis (see Fig. 1b).

The radial velocity at a point $\zeta \in [-1, 1]$ within the element is determined by a linear interpolation of $\dot{r}/r$:

$$\frac{\dot{r}}{r} = \frac{1}{2}(1-\zeta)\frac{\dot{r}_1}{r_1} + \frac{1}{2}(1+\zeta)\frac{\dot{r}_2}{r_2}, \tag{A1a}$$

$$r = \tfrac{1}{2}(1-\zeta)r_1 + \tfrac{1}{2}(1+\zeta)r_2. \tag{A1b}$$

Within each element, two sampling points [34] are introduced at locations specified by $\zeta_{\mathrm{I}} = -\frac{1}{3}\sqrt{3}$ ($r = r_{\mathrm{I}}$) and $\zeta_{\mathrm{II}} = \frac{1}{3}\sqrt{3}$($r = r_{\mathrm{II}}$), respectively (these locations coincide with the 1-D Gaussian integration points). Each sampling point is attributed a volume fraction $v = r/(r_1 + r_2)$, and we define the vectors of generalized element strain-rates and stresses by:

$$\dot{\mathbf{E}} = [D^{\mathrm{I}}_{11}\ D^{\mathrm{I}}_{22}\ 2D^{\mathrm{I}}_{23}\ D^{\mathrm{I}}_{33} \vdots D^{\mathrm{II}}_{11}\ D^{\mathrm{II}}_{22}\ 2D^{\mathrm{II}}_{23}\ D^{\mathrm{II}}_{33}]^T, \tag{A2a}$$

$$\Sigma = V^e[v_{\mathrm{I}}\sigma^{\mathrm{I}}_{11}\ v_{\mathrm{I}}\sigma^{\mathrm{I}}_{22}\ v_{\mathrm{I}}\sigma^{\mathrm{I}}_{23}\ v_{\mathrm{I}}\sigma^{\mathrm{I}}_{33} \vdots v_{\mathrm{II}}\sigma^{\mathrm{II}}_{11}\ v_{\mathrm{II}}\sigma^{\mathrm{II}}_{22}\ v_{\mathrm{II}}\sigma^{II}_{23}\ v_{\mathrm{II}}\sigma^{\mathrm{II}}_{33}]^T, \tag{A2b}$$

where $V^e = \pi(r_2^2 - r_1^2)L$. For quasistatic deformations, the principle of virtual power states, for each of these elements in the current configuration, that:

$$V^e[v_I\boldsymbol{\sigma}_I:\mathbf{D}_I + v_{II}\boldsymbol{\sigma}_{II}:\mathbf{D}_{II}] = \boldsymbol{\Sigma}^T\dot{\mathbf{E}} = \mathbf{F}^T\mathbf{v}.$$

It then follows from Eqn (A2a) with Eqn (14a), along with the principle of virtual power, that:

$$\dot{\mathbf{E}} = \mathbf{D}\mathbf{v}, \quad \mathbf{D}^T\boldsymbol{\Sigma} = \mathbf{F}, \tag{A3}$$

where:

$$\mathbf{D} = [\mathbf{D}_I \ \mathbf{D}_{II}]^T, \tag{A4}$$

$$\mathbf{D}_K = \begin{bmatrix} -(\zeta_K + r_1/b) & (\zeta_K + r_2/b) & 0 & 0 \\ \tfrac{1}{2}(1-\zeta_K)r_K^2 & \tfrac{1}{2}(1+\zeta_K)r_K^2 & 0 & 0 \\ 0 & 0 & r_K^2/L & 0 \\ 0 & 0 & 0 & 1 \end{bmatrix}; \quad K = \mathrm{I}, \mathrm{II}, \tag{A5}$$

with $b = r_2 - r_1$.

The rate equations are derived by straightforward time differentiation of the equilibrium conditions (A3b). Here it may be noted that due to the particular interpolation of the radial velocity field through Eqn (A1a), the sampling points do not coincide with material points; however, this difference may be neglected when the elements are sufficiently small and the total change of the radius of the bar remains small as compared with the initial outer radius $R_{oo}$. After elimination of the stress rates which appear after differentiation by means of the constitutive relations (8), followed by elimination of the strain rates by means of Eqn (A3a), the finite element equations are found of the form:

$$\mathbf{K}\mathbf{v} = \dot{\mathbf{F}} + \mathbf{F}_v, \tag{A6}$$

with:

$$\mathbf{K}\mathbf{D} = \mathbf{D}^T\mathbf{S}\mathbf{D} + \mathbf{G}, \tag{A7a}$$

$$\dot{\mathbf{F}}_v = \mathbf{D}^T\dot{\boldsymbol{\Sigma}}_v. \tag{A7b}$$

Here, the matrix S is determined by the elastic moduli $\mathbf{L}_e$ in the constitutive law (8). Due to symmetry of these moduli, the matrix S is symmetric. The matrix G contains contributions from the geometry dependence of the matrix D in the equilibrium equations (A3b), as well as a contribution from the convective terms appearing in the Jaumann derivative of $\boldsymbol{\sigma}$ in Eqns (7) or (8). It is noted that this G matrix and, as a consequence, the K matrix are nonsymmetric; however, the final simple structure of the K matrix allows for a simple and efficient solution procedure. Furthermore, in Eqn (A7b), $\dot{\boldsymbol{\Sigma}}_v$ is defined in terms of the stress rate $\dot{\boldsymbol{\sigma}}_v$ completely similar to $\boldsymbol{\Sigma}$.